minerals

MDPI

Article

Geochemical Constraints on Antimony Mineralization in the Gutaishan Au–Sb Deposit, China: Insights from Trace Elements in Quartz and Sulfur Isotopes in Stibnite

Jingping Feng [1], Linyan Kang [1,2,*], Bin Li [2] and Peixuan Kang [2]

[1] Natural Resources Survey Institute of Hunan Province, Changsha 410014, China; fengjp123456@163.com
[2] Key Laboratory of Metallogenic Prediction of Nonferrous Metals and Geological Environment Monitoring, Ministry of Education, School of Geosciences and Info-Physics, Central South University, Changsha 410083, China; cutelb@csu.edu.cn (B.L.); 235011003@csu.edu.cn (P.K.)
* Correspondence: kanglinyan@csu.edu.cn

Abstract

The Gutaishan Au–Sb deposit is situated in the southern segment of the Jiangnan Orogenic Belt, a region characterized by a concentration of Au–Sb–W deposits. Previous research has predominantly concentrated on Au mineralization, whereas studies addressing the equally important Sb mineralization are relatively scarce. To investigate key scientific questions regarding the source of ore-forming materials, the physicochemical conditions, and mineralization mechanisms of Sb in the Gutaishan deposit, we conducted systematic analyses of trace elements in hydrothermal quartz and sulfur isotopes in stibnite. Li, Al, Sb, B, Na, K, Ti, Ge, and As are the dominant trace elements in hydrothermal quartz from the Gutaishan deposit. The dominant substitution mechanism is $(Al^{3+}, Sb^{3+}) + (Li^{+}, Na^{+}, K^{+}, H^{+}) \leftrightarrow Si^{4+}$. The relatively low but variable Al concentrations indicate that quartz precipitated from fluids with fluctuating pH and weakly acidic conditions, while variations in Ti and Ge reflect significant temperature changes. These features suggest that fluid mixing was the primary mineralization mechanism in the Gutaishan deposit. Hydrothermal quartz contains anomalously high B concentrations (14.36–30.64 ppm), far exceeding typical hydrothermal levels, while stibnite displays consistent magmatic sulfur isotope signatures (−3.50‰ to −4.2‰, with an average of -3.99 ± 0.2‰), which are markedly different from the in situ $\delta^{34}S$ values of sedimentary sulfides (+7.0‰ to +23.3‰) in the host rocks. This combination of evidence indicates a magmatic–hydrothermal origin for Sb mineralization. Integrating previous geochronological and isotopic constraints with our new observations, we interpret that the Gutaishan deposit represents an intrusion-related Au–Sb deposit formed in a post-collisional extensional setting, where Sb was precipitated after Au mineralization as a result of fluid mixing.

Keywords: hydrothermal quartz; sulfur isotopes; Gutaishan Au–Sb deposit; magmatic-hydrothermal system

check for updates

Academic Editor: Francisco J. González

Received: 21 August 2025
Revised: 2 September 2025
Accepted: 4 September 2025
Published: 6 September 2025

Citation: Feng, J.; Kang, L.; Li, B.; Kang, P. Geochemical Constraints on Antimony Mineralization in the Gutaishan Au–Sb Deposit, China: Insights from Trace Elements in Quartz and Sulfur Isotopes in Stibnite. *Minerals* **2025**, *15*, 953. https://doi.org/10.3390/min15090953

Copyright: © 2025 by the authors. Licensee MDPI, Basel, Switzerland. This article is an open access article distributed under the terms and conditions of the Creative Commons Attribution (CC BY) license (https://creativecommons.org/licenses/by/4.0/).

1. Introduction

The Xiangzhong Au–Sb–W mineralization cluster is located in the southern segment of the Jiangnan Orogenic Belt and constitutes a significant component of the South China metallogenic belt. It serves as a natural laboratory for investigating polymetallic mineralization processes [1,2]. Current research on the Au (–Sb–W) mineralization mechanisms in this area primarily focuses on the Xikuangshan Sb deposit within the Xiangzhong Basin and the

Woxi Au–Sb–W deposit in the Xuefengshan Range, whereas studies on deposits associated with granitoid intrusions remain comparatively scarce. The Gutaishan Au–Sb deposit is a representative Au–Sb deposit situated near the Baimashan granite intrusion. Existing research has primarily focused on Au mineralization [3–9]. For instance, sulfur isotope analyses of sulfides conducted by Wu et al. and Zhang et al. indicate that sulfur in the ores was predominantly derived from deep-seated magmatic sources, with a minor contribution from sedimentary strata [9,10]. Li et al., based on in situ analyses, reported that pyrite and arsenopyrite associated with native gold have $\delta^{34}S$ values of −3.2‰ to +5.7‰ and −3.7‰ to +2.1‰, respectively, which are significantly lower than those of sedimentary pyrite (+7.0‰ to +23.3‰), further suggesting a magmatic origin for sulfur [5]. However, the source of antimony has received little attention in previous studies [7]. Li et al. conducted a comprehensive investigation of quartz from different mineralization stages, employing fluid inclusion petrography, microthermometry, laser Raman spectroscopy, and H–O isotope analyses, along with C–O isotope analyses of siderite closely associated with gold mineralization [11]. Their results suggest that fluid immiscibility, the presence of CH_4-rich gas, sulfidation, and carbonate alteration were key processes responsible for Au precipitation and enrichment. Similarly, Zhou et al. based on fluid inclusion petrography and microthermometry of quartz, also identified fluid immiscibility as the principal mechanism controlling ore precipitation in the Gutaishan area [12]. In contrast, Feng et al. proposed that Au precipitation was primarily driven by fluid boiling, evidenced by the coexistence of aqueous and CO_2-rich fluid inclusions in quartz, their comparable homogenization temperatures, and wide salinity variations [4]. However, the ore-forming mechanisms responsible for Sb mineralization remain poorly constrained. As an important Au-associated mineral, stibnite plays a crucial role in constraining the ore-forming processes. Therefore, investigations into Sb mineralization can provide valuable insights into the metallogenic mechanisms of both Au and Sb mineralization in this deposit.

Quartz is a ubiquitous mineral in igneous, metamorphic, and sedimentary rocks, extensively developed in magmatic–hydrothermal systems, and constitutes one of the most important gangue minerals in antimony deposits [13–15]. In certain ore systems, trace element concentrations in quartz remain consistent over several kilometers, thereby recording large-scale physicochemical conditions rather than localized environmental variations [16–18]. Moreover, quartz is less susceptible to hydrothermal alteration and weathering compared to most hydrothermal minerals [19,20]. Its trace element composition is highly sensitive to the physicochemical parameters of the parent fluid, including temperature, pH, and chemical composition [13,21–23]. Consequently, quartz trace element geochemistry can provide robust constraints on the fluid properties and depositional conditions during quartz crystallization [13,14,24–26]. Specifically, quartz coexisting with stibnite can serve as a valuable proxy for reconstructing the physicochemical environment and ore-forming processes of Sb mineralization.

As the principal ore mineral formed during the Sb mineralization stage of the Gutaishan deposit, stibnite provides critical geochemical constraints on the source of ore-forming materials through its sulfur isotope composition. Sulfur, an essential component of stibnite, typically co-migrates and co-precipitates with antimony [27,28]. Accordingly, the sulfur isotopic composition of stibnite not only reflects the source of sulfur but also serves as an effective proxy for tracing the origin of antimony. Classical mineralogical studies have demonstrated that stibnite exhibits a stable crystal structure and distinctive geochemical properties, making it a reliable mineral phase for investigating ore genesis and fluid characteristics. Sulfur has four stable isotopes (^{32}S, ^{33}S, ^{34}S, and ^{36}S), among which ^{32}S and ^{34}S are most commonly used in geological research. Owing to their characteristic fractionation behavior, sulfur isotopes are highly effective in distinguishing sulfur sources from different

geological reservoirs, including magmatic, sedimentary, and metamorphic origins [29,30]. In particular, $\delta^{34}S$ values exhibit diagnostic ranges for different sources, making sulfur isotopes a reliable tracer for identifying the origin of ore-forming materials [30,31]. Although conventional bulk analytical techniques (e.g., gas-source mass spectrometry) offer high precision, recent advances in laser ablation multi-collector inductively coupled plasma mass spectrometry (LA-MC-ICP-MS) have enabled high–spatial resolution (10–100 μm) in situ sulfur isotope analysis [32–34]. This technique allows single-grain measurements and yields critical geochemical information [32–34]. Consequently, in situ sulfur isotope analysis has seen widespread application in studies of hydrothermal ore deposits, particularly for constraining the source of ore-forming components [35,36].

In this study, we report the trace element compositions of quartz coexisting with stibnite, and in situ sulfur isotope compositions of stibnite from the Gutaishan Au–Sb deposit. These data provide new insights into the physicochemical conditions, ore-forming processes, and sulfur sources involved in Sb mineralization, and contribute to a better understanding of Au–Sb metallogenesis in the Central Hunan metallogenic district.

2. Geological Setting

2.1. Regional Geology

The South China Block was formed by the amalgamation of the Yangtze Block and Cathaysia Block along the Jiangshao Fault Zone during the Neoproterozoic, resulting in the formation of the Jiangnan Orogenic Belt (Figure 1a) [5,37,38]. This orogenic belt hosts the world's largest concentrations of antimony (Sb; reserves of 3.0 Mt, accounting for more than 50% of global reserves), tungsten (WO_3; total reserves of 6.0 Mt), and significant gold (Au; total reserves of 970 t), making it a crucial area for studying metallogenic processes and models [39,40]. The southern segment of the Jiangnan Orogenic Belt exposes strata ranging from the Precambrian to the Quaternary, primarily composed of a basal layer of low-grade metamorphic sedimentary rocks overlain by clastic and carbonate rocks [41]. The Neoproterozoic strata mainly include the Lengjia, Banxi, and Sinian groups, among which the Banxi Group and the volcaniclastic-rich Jiangkou Formation of the Sinian System represent important ore-bearing horizons for Au–Sb mineralization, as exemplified by the Gutaishan and Longshan Au–Sb deposits [41,42]. The protoliths of the Banxi Group mainly consist of sandstones, mudstones, tuffaceous slates, carbonate rocks, volcanic rocks, and volcanic clastic rocks, which underwent regional low-grade metamorphism during the Caledonian orogeny. The Sinian System is dominated by tillites, sandstones, and slates [41,43].

The region has experienced multiple tectonic events, mainly including the Wuling–Xuefeng, Caledonian, Hercynian, and Indosinian–Yanshanian stages, which together produced a structural framework characterized by rift basins (the Lianyuan and Shaoyang basins, which are sub-basins of the Xiangzhong Basin) and a series of uplift zones (the Xuefeng arcuate uplift, Weishan uplift, Baimashan–Longshan uplift, and Miaoerling–Guandimiao uplift) (Figure 1b). The area exhibits well-developed fault systems, primarily NE-trending faults including the Taojiang–Chengbu, Lianyuan–Huangtingshi, and Ningxiang–Xinning faults, as well as NW-trending faults such as the Shaoyang–Chenzhou and Xikuangshan–Lianyuan faults (Figure 1b). The three NE-trending faults divide the EW-trending dome of the Baimashan–Longshan uplift into three parts: Baimashan, Dachengshan, and Longshan (Figure 1b) [10]. Among these tectonic events, the Caledonian and Indosinian orogenies were most closely associated with metallogenesis in the southern Jiangnan Orogenic Belt, both accompanied by large-scale granitoid intrusions. Accordingly, the Jiangnan Orogenic Belt is dominated by Devonian and Triassic granites, such as the Baimashan, Weishan, Guandimiao, Taojiang, and Ziyunshan plutons (Figure 1b). The

Baimashan pluton, the largest in the region, underwent magmatic events during the Late Silurian (422.0–411.8 Ma), Triassic (233–204.5 Ma), and Early Jurassic (176.0 ± 4.4 Ma), and it can be subdivided into the Shuichechao unit (~420 Ma) and the Xiaosajiang unit (240–220 Ma) (Figure 1b) [44–47].

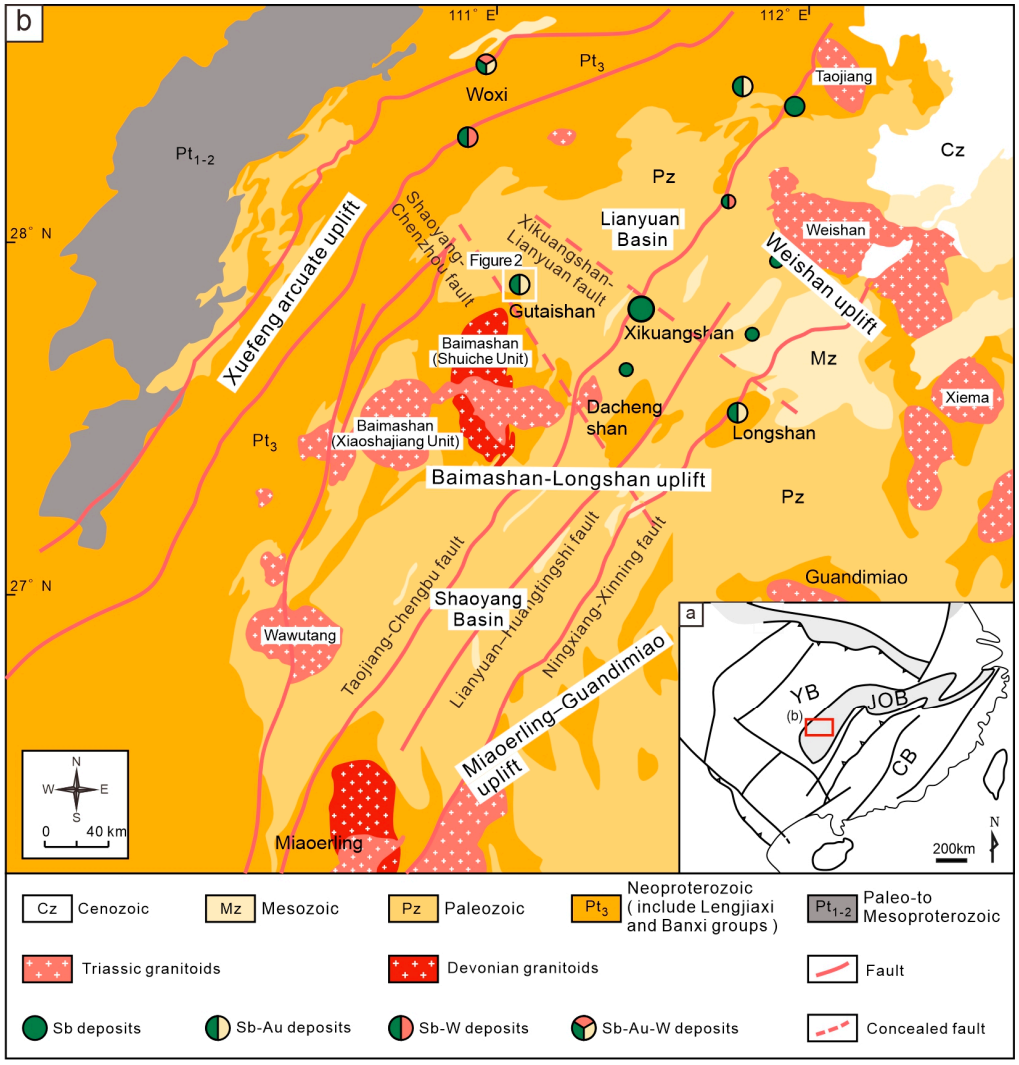


Figure 1. (**a**) The location diagram of the south segment of the Jiangnan Orogenic Belt in the structural framework of South China block (modified after [38]). (**b**) Regional geological map of the distribution of important Sb-Au-W deposits in the south segment of the Jiangnan Orogenic Belt, showing the location of the Gutaishan Au–Sb deposit (modified after [4,11]). YB–Yangtze Block; CB–Cathaysia Block; JOB–Jiangnan Orogen Belt.

2.2. Deposit Geology

The Gutaishan Au–Sb deposit is situated at the intersection of the EW-trending Baimashan–Longshan uplift zone and the Xuefengshan arcuate structural belt, on the northeastern periphery of the Baimashan pluton (Figure 1). Proven reserves include approximately 9 tonnes of gold with an average grade of 13 g/t, and 2500 tonnes of antimony with an average grade of 10% [5]. The regional stratigraphy mainly comprises the Banxi Group, Sinian System, Cambrian System, and Upper Ordovician strata (Figure 2). Among these, the Wuqiangxi Formation of the Banxi Group and the Jiangkou Formation of the Sinian System are the primary ore-bearing host rocks [11]. The Wuqiangxi Formation mainly consists of gray-green chlorite–sericite schists, bluish-gray banded sandy schists, and sandstones [11]. The Jiangkou Formation is characterized by purple sandy schists,

gray conglomerate-bearing fine sandstone schists, and intercalated metamorphosed siltstones [11]. The deposit area lacks significant folding; the primary structures are faults, categorized by strike into four groups: NE-, NW-, NS-, and near EW-trending faults. Mineralization is predominantly controlled by northwest-trending faults, which act as critical ore conduits and host structures [48,49]. Extensive wall-rock alteration occurs within the deposit, including sulfidation (characterized by the presence of pyrite and arsenopyrite), silicification, carbonatization, sericitization, and chloritization. The Au–Sb mineralization is closely linked to sulfidation, silicification, and sericitization [5,6]. Muscovite $^{40}Ar/^{39}Ar$ dating constrains the Au mineralization age in Gutaishan deposit to approximately 223.6 ± 5.3 Ma, contemporaneous with the nearby Baimashan granite intrusion (223–204 Ma), suggesting a possible genetic link to Late Triassic magmatism [5]. Approximately 2 km southwest of the deposit, the composite Baimashan pluton is exposed, accompanied by minor outcrops of granites of undetermined age (Figure 2).

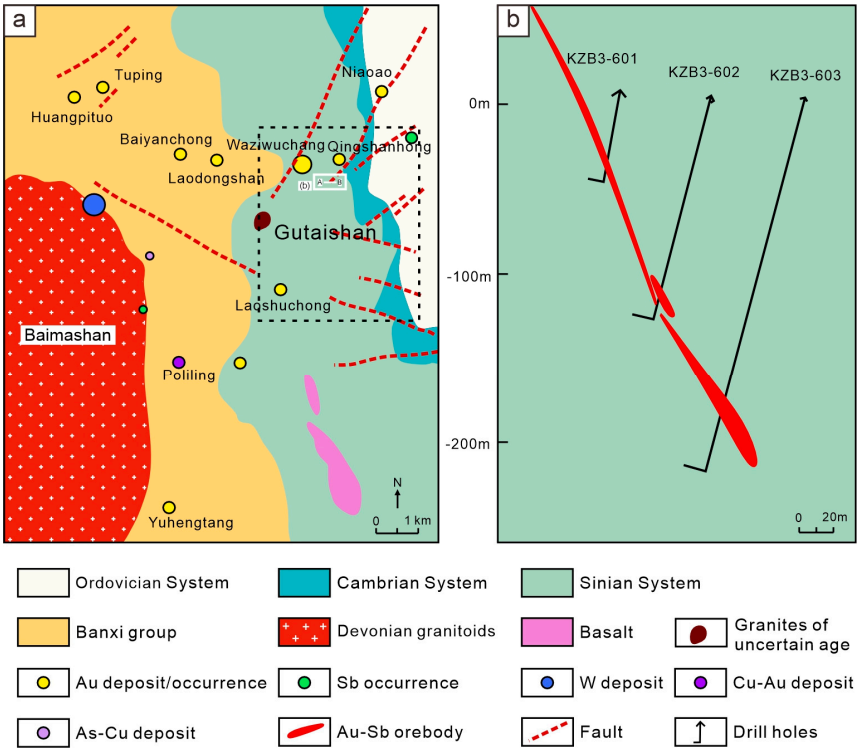


Figure 2. (**a**) Geological schematic map of the Gutaishan Au–Sb deposit (modified after [7]). (**b**) Geological Cross-section of the Gutaishan Au–Sb Deposit along A–B in (**a**) (modified after [49]).

Previous studies have classified the mineral paragenesis of the Gutaishan deposit into four stages: (1) pyrite–quartz stage; (2) quartz–ankerite–sulfide vein stage; (3) main Au–Sb mineralization stage; and (4) quartz stage [7]. The third stage, which contains the majority of Sb reserves, is considered the critical period for Sb mineralization research [7]. Stage one is characterized by pyrite layers parallel to sedimentary bedding and deformed segregated quartz veins ranging from several centimeters to tens of centimeters in thickness. Stage two comprises quartz–ankerite–sulfide veins, typically 1 to 20 cm wide. The third stage is distinguished by dense auriferous quartz veins within the schists. These veins are categorized into four types based on mineral assemblages: (i) quartz with stibnite, pyrite, ankerite, and visible gold; (ii) quartz with ankerite and minor visible gold; (iii) quartz with minor stibnite, pyrite, and visible gold; and (iv) quartz with stibnite and minor pyrite and rare visible gold [5]. The type (iv) veins from third stage correspond to the samples analyzed in this study (Figure 3a).

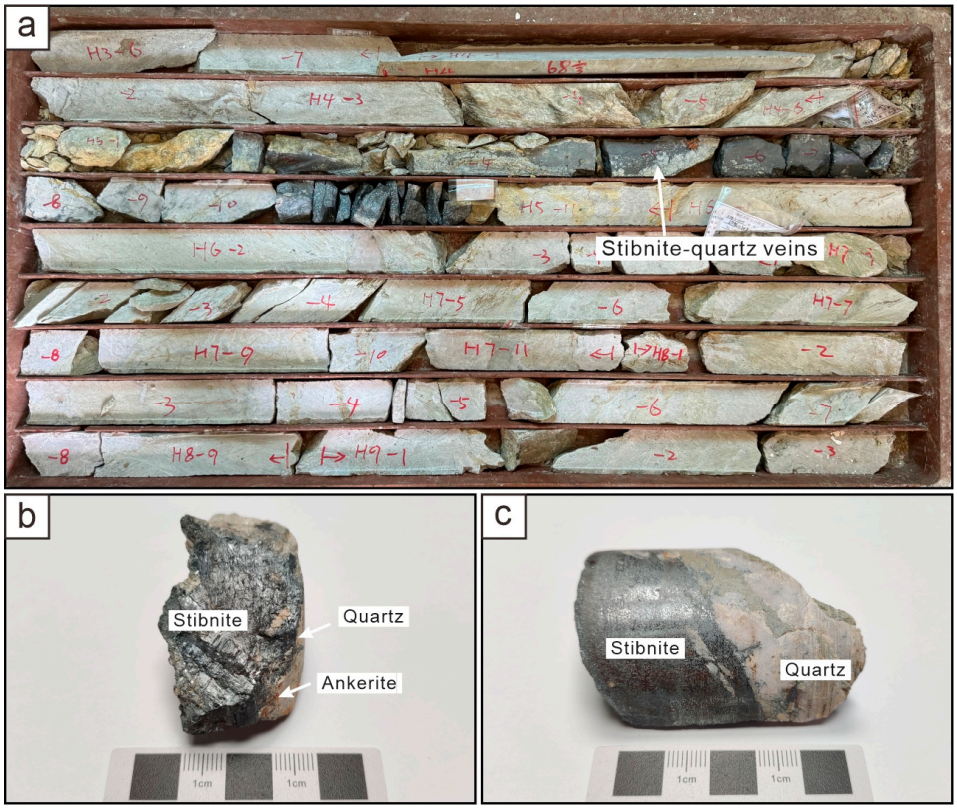


Figure 3. (**a**) Drill core samples from Gutaishan Au–Sb deposit, stored in standard core box. (**b**,**c**) Hand specimen of ores from Au–Sb deposit.

3. Samples and Analytical Methods

In this study, samples were primarily collected from the third-stage Au–Sb mineralization stage of the Gutaishan Au–Sb deposit. All samples were obtained from drill cores KZB3-1001 and KZB3-209, covering depths ranging from 30 m to 113 m (Figure 3a). The main ore minerals include stibnite and pyrite, with minor native gold, while the dominant gangue minerals are quartz and ankerite (Figures 3b,c and 4a–d). The collected samples were prepared as thin sections and polished probe mounts for subsequent analyses. In situ trace element analyses were conducted on hydrothermal quartz coexisting with stibnite, and sulfur isotope analyses were performed on representative stibnite grains.

Trace element compositions of hydrothermal quartz were determined by femtosecond laser ablation inductively coupled plasma mass spectrometry (fs-LA-ICP-MS) at the State Key Laboratory of Continental Dynamics, Northwest University, China. The measured elements included Li, B, Na, Al, K, Ca, Ti, Ge, Ga, Sr, Rb, Ba, Sb, and As. A femtosecond laser system was coupled with an Agilent 7900 ICP-MS for analysis. Helium was employed as the carrier gas, while argon served as the auxiliary gas. Each analytical run consisted of 20 s of background measurement, followed by 45 s of laser ablation, and 40 s for signal washout. Quantification was achieved using NIST SRM 610 as the external reference material and Si as the internal standard. Certified reference materials BCR-2G, BHVO-2G, and NIST SRM 610 were routinely analyzed to monitor the accuracy and reproducibility of the results [50]. The raw data were processed using the internal standard method with ICPMSDataCal version 12.2 [51].

In situ sulfur isotope analyses of stibnite were performed at the State Key Laboratory of Continental Dynamics, Northwest University, China, utilizing a RESOlution M-50 193 nm Arve excimer laser ablation system (ASI) coupled to a Nu Plasma 1700 multi-collector inductively coupled plasma mass spectrometer (MC-ICP-MS). The laser system

was equipped with a dual-volume ablation cell, a high-precision motorized X–Y stage, and a computer-controlled sample positioning unit, which collectively enhanced both spatial resolution and analytical efficiency. Analytical parameters were set to an energy density of 3.6 J/cm^2, a repetition rate of 3 Hz, and a spot diameter ranging from 25 to 37 µm. All analyses were conducted in single-spot ablation mode. High-purity helium was introduced at a flow rate of 280 mL/min as the carrier gas, while argon was supplied at 0.86 L/min as the auxiliary gas. Sulfur isotopic ratios (^{32}S, ^{33}S, and ^{34}S) were measured simultaneously in static collection mode, using the L4, Ax, and H5 Faraday collectors, respectively. Data were acquired in time-resolved analysis (TRA) mode with an integration time of 0.2 s, consisting of three segments: a 30-s background signal acquisition, a 50-s ablation signal acquisition, and a 75-s system washout. Detailed analytical protocols closely followed those described by Chen et al. and Bao et al. [52,53]. A standard–sample–standard bracketing sequence (SSB method) was implemented throughout the analysis to correct for instrumental drift and ensure accuracy in measured ^{34}S/^{32}S ratios. Given the strong matrix effects intrinsic to laser ablation MC-ICP-MS, matrix-matched sulfide standards were used, including sphalerite NBS123 (17.8 ± 0.2‰) and pyrite Py-4 (1.7 ± 0.3‰). To monitor analytical precision and instrument stability, one pair of standards was analyzed following every eight unknown samples.

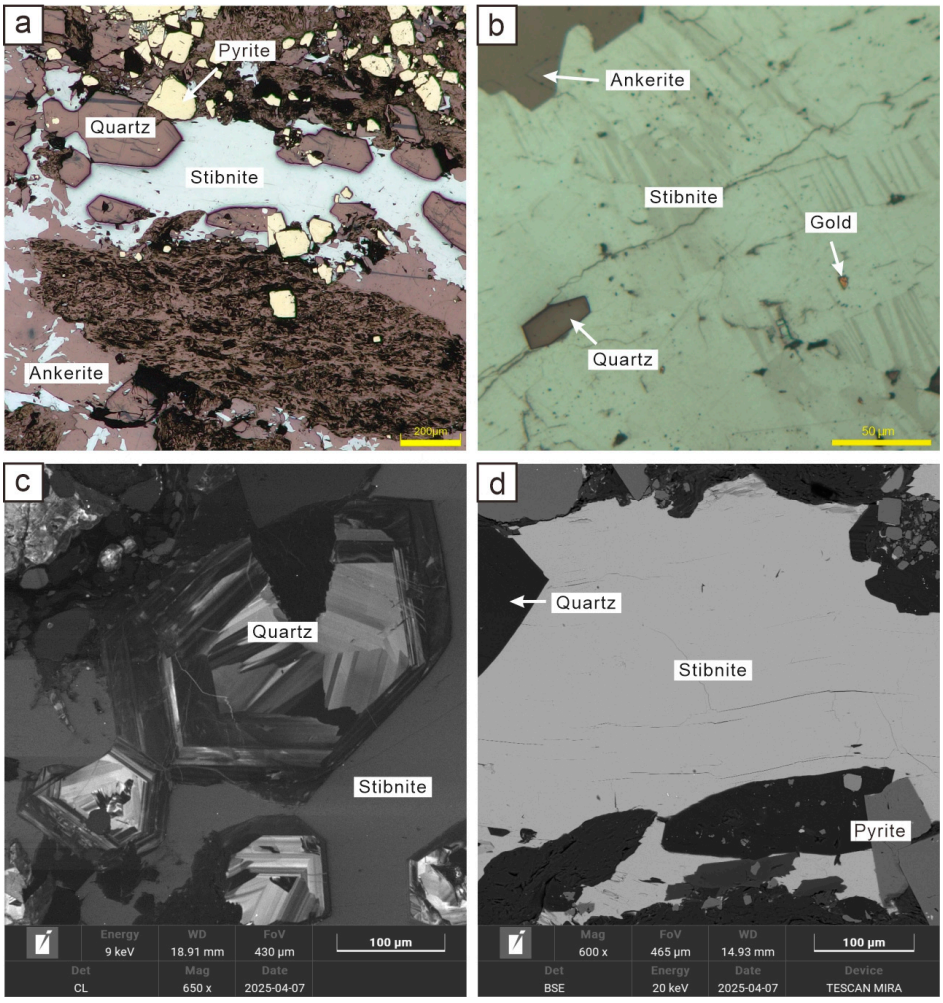


Figure 4. Microscopic microphotographs of minerals in ores from Gutaishan Au–Sb deposit. (**a**,**b**) Reflection micrograph. (**c**) The structure of quartz in the SEM-CL image. (**d**) BSE image of stibnite.

4. Results

4.1. Trace Element Composition of Quartz

A total of 34 spot analyses were conducted on quartz grains associated with stibnite. The complete trace element data obtained by fsLA-ICP-MS are provided in Supplementary Table S1, and selected elements with relatively high concentrations are shown in Figure 6. The results indicate that Li, Al, Sb, B, Na, K, Ti, Ge, and As are the most abundant trace elements in quartz from the Gutaishan deposit. For comparison, trace element data of quartz coexisting with stibnite from the Woxi Au–Sb–W deposit were also included in this study (Figure 5) [54]. Similar to Gutaishan, the Woxi deposit is located in the southern segment of the Jiangnan Orogen. However, it lies within the Xuefengshan region and is characterized by the absence of exposed granitic intrusions in the vicinity. Therefore, it has been classified as an orogenic-type deposit [2,54,55]. The data show that quartz from the Gutaishan and Woxi deposits generally exhibits similar trace element compositions (Figure 5). Nevertheless, the B content in quartz from Gutaishan deposit is significantly higher than that in quartz from the Woxi deposit.

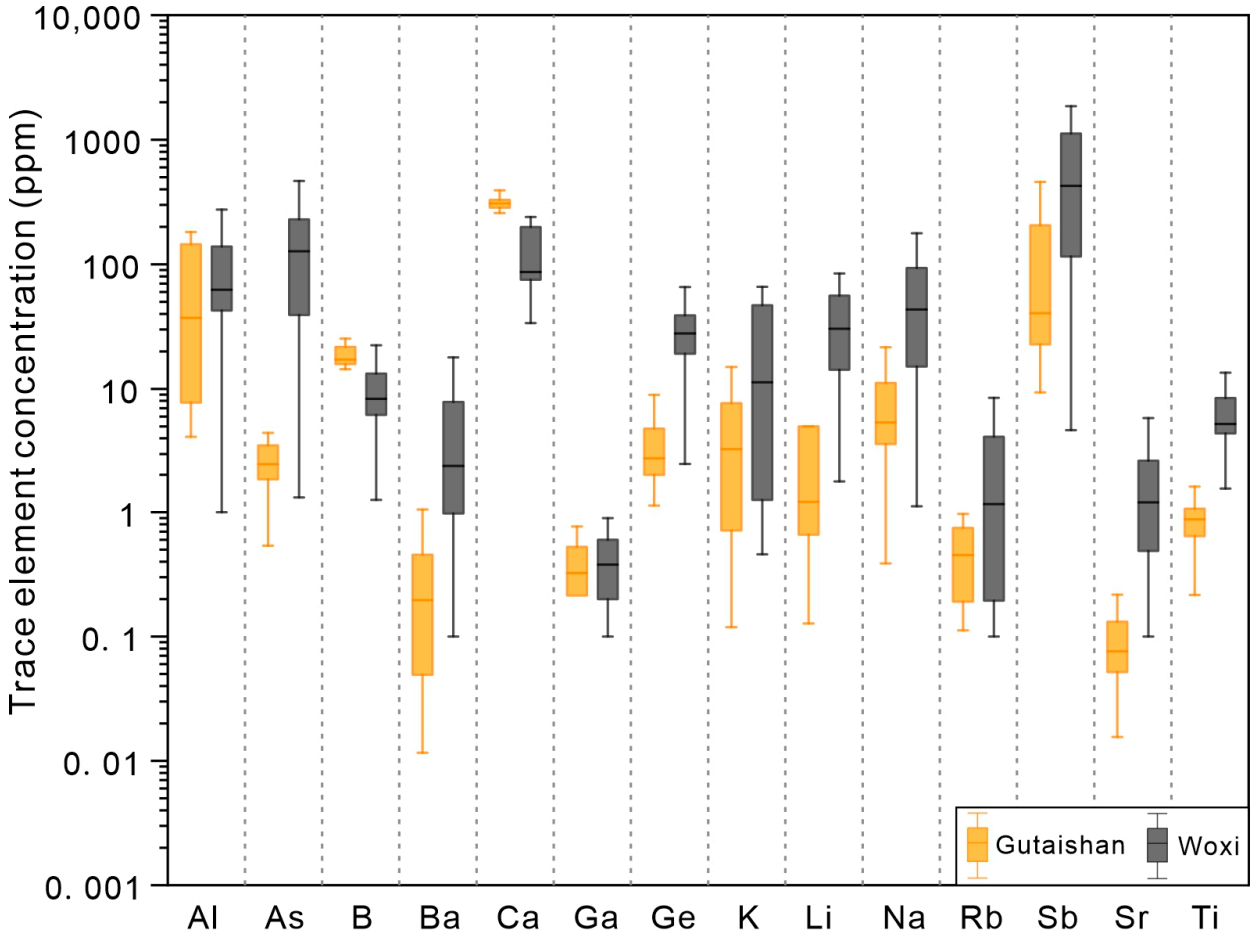


Figure 5. Box diagram of trace element content in hydrothermal quartz of Gutaishan and Woxi deposit.

To evaluate the incorporation mechanisms of trace elements into the quartz lattice, the measured concentrations were converted to atoms per formula unit (p.f.u.), on the basis of one silicon atom per formula unit. This normalization facilitates comparisons among different trace elements and helps identify potential charge-balanced substitution mechanisms (e.g., Al^{3+} replacing Si^{4+}, with charge compensation by Li^{+}, Na^{+}, or H^{+}). The normalized results are presented in Supplementary Table S2.

4.2. Sulfur Isotopic Composition of Stibnite

Twenty in situ sulfur isotope analyses were conducted on stibnite from the Gutaishan Au–Sb deposit, and the results are presented in Table 1. The $\delta^{34}S$ values of stibnite exhibit a narrow range from −4.42‰ to −3.50‰, with a mean of −3.99 ± 0.2‰ (n = 20, σ).

Table 1. In situ sulfur isotopic compositions ($\delta^{34}S$) of stibnite from the Gutaishan Au–Sb deposit.

Sample Name	Sample Types	Minerals	$^{34}S_{V\text{-}CDT}$	1σ
K2B3-1001-1-1	Stibnite ores	Stibnite	−4.42	0.17
K2B3-1001-1-2	Stibnite ores	Stibnite	−4.19	0.18
K2B3-1001-1-3	Stibnite ores	Stibnite	−4.13	0.18
K2B3-1001-1-4	Stibnite ores	Stibnite	−4.22	0.18
K2B3-1001-1-5	Stibnite ores	Stibnite	−4.43	0.20
K2B3-1001-1-6	Stibnite ores	Stibnite	−4.27	0.16
K2B3-1001-1-7	Stibnite ores	Stibnite	−4.05	0.17
K2B3-1001-1-8	Stibnite ores	Stibnite	−4.36	0.19
K2B3-1001-1-9	Stibnite ores	Stibnite	−4.08	0.18
K2B3-1001-1-10	Stibnite ores	Stibnite	−4.46	0.18
K2B3-209-1-1	Stibnite ores	Stibnite	−3.80	0.18
K2B3-209-1-2	Stibnite ores	Stibnite	−3.77	0.21
K2B3-209-1-3	Stibnite ores	Stibnite	−3.68	0.21
K2B3-209-1-4	Stibnite ores	Stibnite	−3.95	0.19
K2B3-209-1-5	Stibnite ores	Stibnite	−3.51	0.22
K2B3-209-1-6	Stibnite ores	Stibnite	−3.85	0.18
K2B3-209-1-7	Stibnite ores	Stibnite	−3.87	0.17
K2B3-209-1-8	Stibnite ores	Stibnite	−3.61	0.17
K2B3-209-1-9	Stibnite ores	Stibnite	−3.50	0.17
K2B3-209-1-10	Stibnite ores	Stibnite	−3.76	0.17

5. Discussion

5.1. Substitution Mechanisms of Trace Elements in Quartz

Quartz possesses a dense Si–O tetrahedral framework that generally limits the incorporation of other elements into its crystal lattice [56]. Nevertheless, certain trace elements can substitute for Si^{4+} through coupled substitution mechanisms [18,57,58]. Among these, Al^{3+} is the most common substituent due to its abundance in the crust and its ionic radius, which is comparable to that of Si^{4+}. To maintain charge balance, monovalent cations such as Li^+, Na^+, K^+, Ag^+, and H^+ are typically involved as charge compensators [59–61]. In quartz from the Gutaishan deposit, Al^{3+} exhibits elevated concentrations and a strong negative correlation with Si^{4+} (Figure 6a), indicating its substitution for Si. Meanwhile, Li, Na, and K concentrations increase concomitantly with Al, consistent with their role as charge-balancing cations. The strong positive correlation between Li^+ and Al^{3+} is particularly evident (Figure 6b). Besides Al^{3+}, other elements such as B^{3+}, Fe^{3+}, Sb^{3+}, Ti^{4+}, Ge^{4+}, and P^{5+} are also capable of substituting for Si^{4+} [21,62,63]. The observed positive correlations of Sb^{3+} with Al^{3+} and Li^+ (Figure 6c,e), along with a negative correlation with Si^{4+} (Figure 6d), suggest that Sb^{3+} is also structurally incorporated into quartz. The relatively smooth and continuous fsLA-ICP-MS signal profiles of Sb further support a homogeneous distribution within the quartz lattice rather than the presence of Sb-bearing inclusions or contamination. Although the sum of Al^{3+} and Sb^{3+} (M3) correlates well with that of Li^+, Na^+, and K^+ (M1) (Figure 6f), the monovalent cations are slightly deficient, implying the involvement of H^+ as an additional charge-balancing ion [13,64,65]. Overall, the dominant trace-element substitution mechanism in quartz from this deposit can be expressed as $(Al^{3+}, Sb^{3+}) + (Li^+, Na^+, K^+, H^+) \leftrightarrow Si^{4+}$.

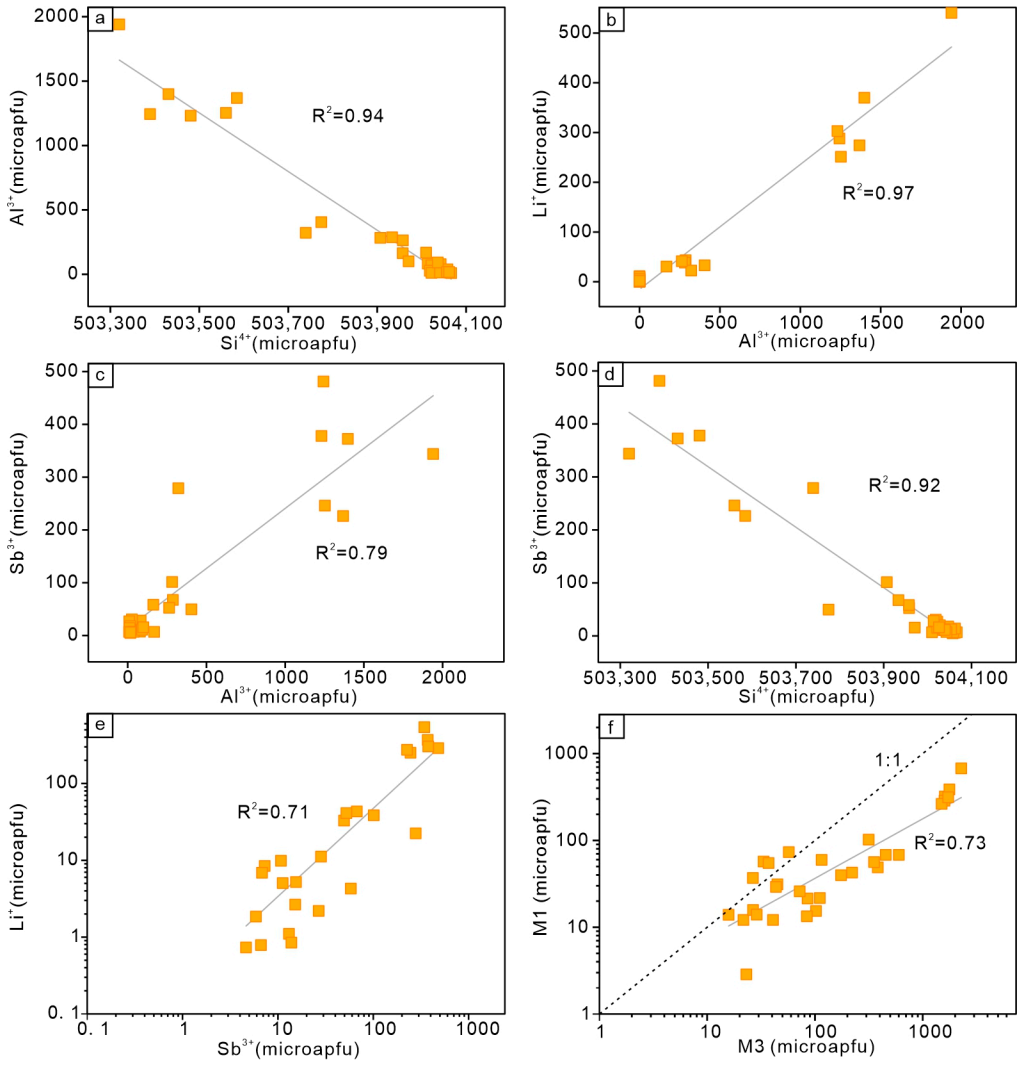


Figure 6. Relationship of trace element ions in hydrothermal quartz of Gutaishan deposit. (**a**) Al^{3+} vs. Si^{4+}; (**b**) Li^{+} vs. Al^{3+}; (**c**) Sb^{3+} vs. Al^{3+}; (**d**) Sb^{3+} vs. Si^{4+}; (**e**) Li^{+} vs. Sb^{3+}; (**f**) M1 vs. M3. M1: Li^{+}, Na^{+}, and K^{+}. M3: Al^{3+} and Sb^{3+}.

5.2. Genesis of the Gutaishan Au–Sb Deposit

The trace element characteristics of quartz can provide insights into the physicochemical conditions of the mineralizing fluid and the environment during quartz precipitation [14,18,24,66]. Among these elements, Al concentration is commonly regarded as an indicator of fluid pH. Specifically, as a trivalent cation, Al tends to substitute for Si more readily under relatively acidic conditions; thus, higher Al content in quartz typically reflects a more acidic mineralizing fluid [13,18]. This relationship is particularly pronounced in low-temperature hydrothermal systems [13,18]. In the Gutaishan deposit, quartz exhibits relatively low Al concentrations (generally below 1000 ppm) with significant variability (ranging from less than 10 to 1000 ppm), indicating precipitation from a fluid with weak acidity and notable pH fluctuations (Figure 5). Besides Al, Ti and Ge contents in quartz serve as proxies for fluid temperature during quartz formation. When the solubility of Ti and Ge in the fluid decreases, it reflects a drop in temperature, which consequently results in lower concentrations of these elements in quartz [14,24,67]. The variable Ti and Ge contents in quartz from the Gutaishan deposit suggest that quartz precipitation occurred under conditions with considerable temperature fluctuations (Figure 5). Based on the trace element characteristics, it is evident that the mineralizing fluids experienced significant

fluctuations in pH and temperature during precipitation. These variations cannot be solely explained by fluid boiling or cooling, suggesting that fluid mixing played a crucial role in the formation of quartz and stibnite (this study), consistent with previous H-O isotope evidence from quartz [11,12].

5.3. Magmatic–Hydrothermal Contributions to Sb Mineralization

The B concentration in hydrothermal quartz is typically less than 1 ppm [68]. However, in hydrothermal quartz from the Gutaishan deposit, B concentrations range from 14.36 to 30.64 ppm, which is considerably higher than those commonly observed in hydrothermal quartz (less than 1 ppm), such as quartz from the Woxi deposit (Figure 5). Although most other trace elements (e.g., As, Ba, Ti) are more enriched in quartz from Woxi deposit, this likely reflects the distinct geochemical characteristics of typical orogenic deposits [54]. In contrast, the notable enrichment of B in quartz from the Gutaishan deposit indicates that the mineralizing fluids were B-rich. Although high-salinity fluids can stabilize boron-bearing complexes [69], the Gutaishan fluids are characterized by medium to low salinity. The positive correlation between B and Al concentrations further indicates that B was structurally incorporated into the quartz lattice rather than occurring as fluid inclusions. Its enrichment in quartz most plausibly reflects the exsolution of B-rich fluids from evolved magmas during the late stages of crystallization, which subsequently participated in quartz precipitation. This interpretation is supported by quartz trace-element systematics: in the Al/50-Ti-Ge × 10 ternary diagram (Figure 7), most hydrothermal quartz samples plot within the compositional fields of pegmatitic quartz, indicating the transition from magmatic to hydrothermal fluids [70–72], which also supports the genetic link between the deposit and a magmatic–hydrothermal system. Collectively, the elevated B concentrations, together with trace-element systematics, provide robust evidence for a magmatic contribution to the ore-forming fluid.

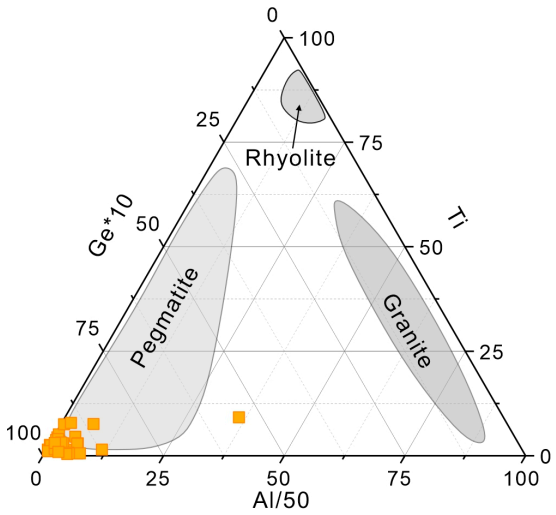


Figure 7. Al/50-Ti-Ge × 10 ternary diagram of hydrothermal quartz from the Gutaishan Au–Sb deposit (in ppm). Quartz data from rhyolite, pegmatite, and granite are plotted for comparison (after [70]).

Stibnite is the dominant sulfide mineral in the Gutaishan deposit, rendering the presence of other sulfide minerals such as pyrite negligible in comparison [31]. Moreover, stibnite generally forms under relatively low temperatures, low oxygen fugacity (fO^2), and acidic to neutral conditions [73,74]. Under these circumstances, sulfur isotope fractionation between the fluid and sulfide minerals is minimal [74]. Consequently, the $\delta^{34}S$ values of stibnite can be considered an approximate representation of the original sulfur

isotopic composition of the ore-forming fluid [31]. Magmatic sulfur typically ranges from 0 ± 5‰ [75], seawater sulfur from +15‰ to +21‰ [76], and biogenic sulfur from –50‰ to –20‰ (Figure 8) [29]. In this study, in situ $\delta^{34}S$ analyses of stibnite from the deposit reveal a narrow range of values (−3.50 to −4.2‰), with an average of −3.99 ± 0.2‰, which falls within the typical range for magmatic sulfur (Figure 8). Additionally, these $\delta^{34}S$ values significantly differ from those of sedimentary pyrite in the Banxi Group strata (Figure 8) (+7.0 to +23.3‰), further supporting a magmatic sulfur source (Figure 8) [5]. Consistently, sulfur isotope data from pyrite and arsenopyrite within the same deposit also point to magmatic sulfur as the primary source (Figure 8) [5]. This evidence suggests a shared sulfur origin for both Sb and Au mineralization in the deposit. Furthermore, geophysical studies indicate the possible existence of a concealed intrusion at depth beneath the Gutaishan deposit [77]. Taken together with the trace element characteristics of hydrothermal quartz described above, these observations imply that the deposit is related to a magmatic–hydrothermal system, with mineralizing materials derived from magmatic–hydrothermal fluids.

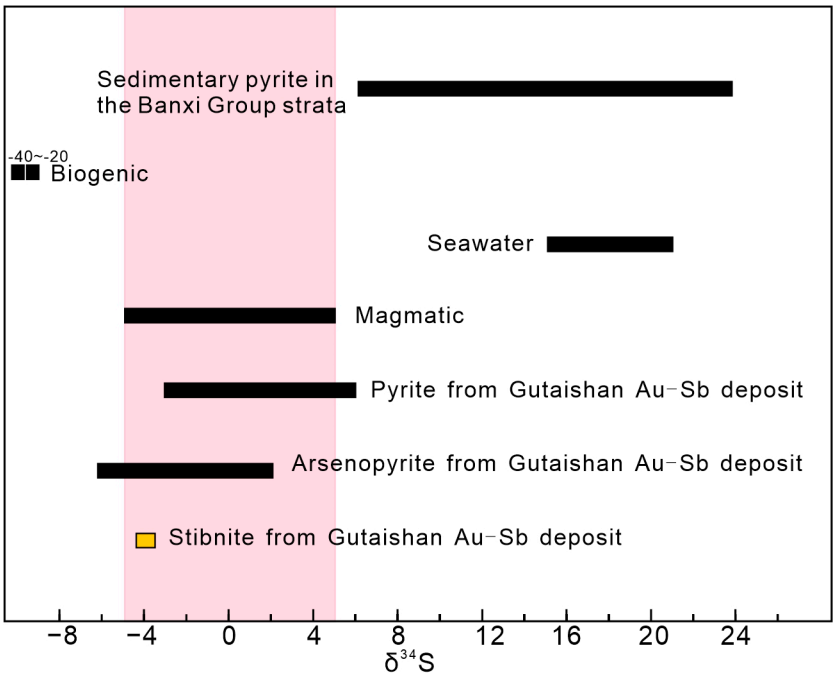


Figure 8. Sulfur isotopic comparison of sulfide minerals in the Gutaishan Au–Sb deposit. Data sources: Magmatic sulfur from [75], seawater sulfur from [76], biogenic sulfur from [29], Sedimentary pyrite in the Banxi Group strata, pyrite, and Arsenopyrite from [5]. The pink field represents the range of magmatic sulfur, and the yellow bar denotes the sulfur isotopic data of stibnite obtained in this study.

5.4. Mineralization Model of the Gutaishan Au–Sb Deposit

Systematic variations in Al and Ti concentrations from about 30 hydrothermal quartz samples across different deposits have established characteristic trace element signatures for quartz from epithermal, orogenic, and porphyry deposits, demonstrating that trace element compositions of quartz alone can effectively discriminate deposit types [13]. For the hydrothermal quartz samples from the Gutaishan deposit, the Al and Ti contents (Al: 100–1000 ppm; Ti: 1–10 ppm) are closely comparable to those typical of orogenic deposits (Figure 9). However, in complex polymetallic systems, trace element characteristics of quartz alone are insufficient to comprehensively classify deposit types. For example, the trace element characteristics of quartz from the Woxi deposit overlap with those of both orogenic and porphyry deposits (Figure 9), whereas its ore-forming fluids exhibit low temperature, low salinity, and enrichment in CO_2 and N_2, consistent with fluid traits

of orogenic Au deposits [55]. Moreover, Sm-Nd and $^{40}Ar/^{39}Ar$ dating indicate that the Woxi mineralization occurred around 400 Ma [78], corresponding to the Late Caledonian intracontinental orogeny in the Xuefengshan region. Given the absence of exposed igneous rocks and direct evidence of magmatic–hydrothermal activity in Woxi, it has been classified as an orogenic Au deposit [54]. In contrast, the Gutaishan deposit displays mineralogical (quartz, arsenopyrite, pyrite, stibnite), host rock alteration (pyritization, arsenopyritization, silicification), and ore-forming fluid characteristics (medium to low temperature, low salinity, CO_2-rich) [4,10], which are consistent with orogenic Au deposits. However, the classical orogenic gold deposit model suggests that ore-forming materials and fluids are mainly derived from metamorphic devolatilization and that mineralization typically occurs close in time to metamorphism [79,80]. In contrast, the H-O isotopic signatures of quartz indicate that the ore-forming fluids were predominantly magmatic in origin [11]. Moreover, the trace element characteristics of quartz and sulfur isotopes of stibnite suggest that the ore-forming materials were mainly sourced from magmatic–hydrothermal fluids (this study). Muscovite $^{40}Ar/^{39}Ar$ dating constrains the Au mineralization age of the Gutaishan deposit to approximately 223.6 ± 5.3 Ma, which is significantly younger than the Caledonian metamorphism [5]. Furthermore, the mineralization is temporally coeval with the emplacement of the nearby Baimashan granite intrusion (223–204 Ma), an I-type granite derived from crustal sources and emplaced in a post-collisional extensional tectonic setting [81]. Therefore, despite the similarity of quartz trace elements (Al and Ti) in Gutaishan deposit to those in orogenic deposits, this likely reflects comparable crystallization conditions rather than genetic similarity. Integrating geochronological, isotopic, and geochemical evidence, the Gutaishan deposit demonstrates a close temporal and genetic link with the Baimashan granite and is best classified as an intrusion-related Au–Sb deposit, distinct from typical orogenic gold deposits.

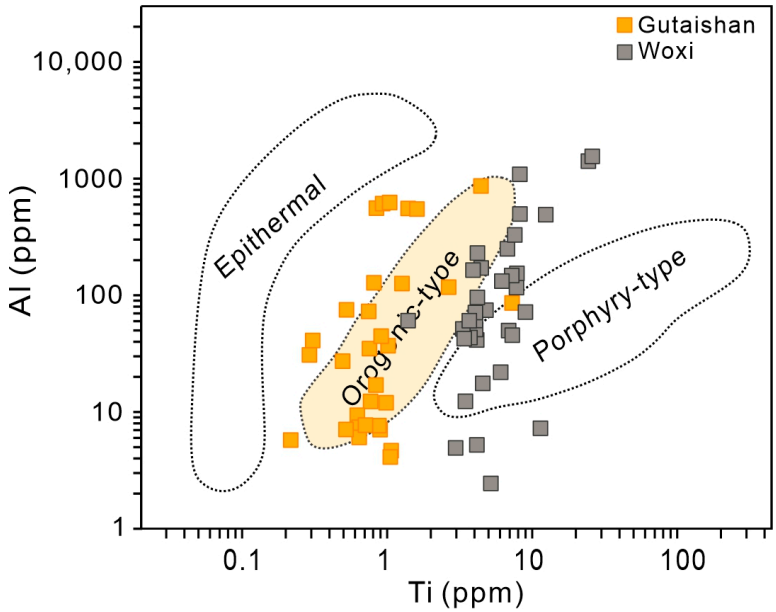


Figure 9. Al vs. Ti concentrations in hydrothermal quartz from the Gutaishan Au–Sb deposit (logarithmic scale), compared with quartz from epithermal, orogenic, and porphyry deposits [13]. Additional data from the Woxi deposit are from [54]. Trace elements in quartz compositions distinguish these deposit types. Porphyry-related quartz is typically Ti-rich, epithermal quartz shows low Ti but variable Al, and orogenic quartz occupies an intermediate range.

Combining quartz trace element features with previous fluid inclusion studies, it can be inferred that the Gutaishan deposit was associated with moderately low-temperature,

weakly acidic fluids, which provided favorable conditions for co-transport of Sb and Au. Since gold solubility is more sensitive to temperature than stibnite, gold precipitation occurred earlier and at higher temperatures than stibnite [82]. Thus, we propose a two-stage mineralization model for Gutaishan Au–Sb deposit: an early Au-dominated stage followed by a later stibnite-dominated stage, consistent with previously defined mineralization stages based on mineral paragenesis and cross-cutting relationships. However, precise dating of the Sb mineralization is still lacking and requires further constraint. Precise dating of Sb mineralization is essential for better understanding the Au–Sb mineralizing system and the relative timing of gold and stibnite precipitation. Multistage mineralization has been recognized as critical in many large gold deposits [83–86]. Recent research on the nearby Longshan deposit within the same tectonic belt also indicates a two-stage mineralization process [87]. Therefore, we infer that, in the Late Triassic post-arc extensional setting, magmatic–hydrothermal activity first drove gold precipitation, followed by stibnite formation promoted by fluid mixing, ultimately producing the composite Au–Sb mineralization observed in the Gutaishan deposit.

6. Conclusions

(1) Quartz associated with stibnite from the Gutaishan Au–Sb deposit records a trace element substitution mechanism: $(Al^{3+}, Sb^{3+}) + (Li^{+}, Na^{+}, K^{+}, H^{+}) \leftrightarrow Si^{4+}$.

(2) The concentrations and variations in Al, Ti, and Ge in quartz reflect significant pH and temperature fluctuations of the ore-forming fluids during precipitation, suggesting that fluid mixing was the key mechanism for stibnite deposition.

(3) The anomalously high B contents in hydrothermal quartz (14–31 ppm), together with trace-element systematics and $\delta^{34}S$ values of stibnite (–3.99‰), reveal a genetic link between the magmatic–hydrothermal system and Sb mineralization.

(4) The Gutaishan deposit is an intrusion-related Au–Sb deposit. Mineralization occurred in a post-collisional extensional setting during the late Indosinian orogeny, comprising an early Au-dominated stage followed by a later Sb-dominated stage triggered by fluid mixing.

Supplementary Materials: The following supporting information can be downloaded at: https://www.mdpi.com/article/10.3390/min15090953/s1, Table S1: fsLA-ICP-MS trace element compositions (ppm) of quartz from the Gutaishan Au–Sb deposit; Table S2: Converting the trace element contents of quartz into atoms per formula units.

Author Contributions: Contributions: All authors contributed to the study conception and design. J.F.: Investigation, sample preparation, data curation, formal analysis, conceptualization, writing—original draft, visualization. L.K.: Investigation, conceptualization, formal analysis, writing—review & editing, project administration. B.L.: Investigation, writing—review & editing, resources, project administration, supervision, funding acquisition. P.K.: Investigation, formal analysis, writing—review & editing. All authors have read and agreed to the published version of the manuscript.

Funding: This study was supported by the National Natural Science Foundation of China (42372105 and 42073001), the Major Scientific Research Program of the Geological Bureau of Hunan Province (HNGSTP202305), the Major Scientific and Technological Research Project of the Hunan Provincial Department of Natural Resources (Xiangzizike [2022] No. 2), the Key Scientific Research Program of Geological Bureau of Hunan Province (HNGSTP202508), and the Youth Talent Program of Geological Bureau of Hunan Province (HNGSTP202326).

Data Availability Statement: The data on trace elements have been added in the supplementary material file.

Conflicts of Interest: The authors declare no conflicts of interest.

References

1. Ding, J.; Zhang, Y.; Ma, Y.; Wang, Y.; Zhang, J.; Zhang, T. Metallogenic characteristics and resource potential of antimony in China. *J. Geochem. Explor.* **2021**, *230*, 106834. [CrossRef]
2. Peng, J.T.; Hu, R.Z.; Burnard, P.G. Samarium–neodymium isotope systematics of hydrothermal calcites from the Xikuangshan antimony deposit (Hunan, China): The potential of calcite as a geochronometer. *Chem. Geol.* **2003**, *200*, 129–136. [CrossRef]
3. Feng, Y.; Zhang, Y.; Xie, Y.; Shao, Y.; Lai, C. Pyrite geochemistry and metallogenic implications of Gutaishan Au deposit in Jiangnan Orogen, South China. *Ore Geol. Rev.* **2020**, *117*, 103298. [CrossRef]
4. Feng, Y.; Zhang, Y.; Xie, Y.; Shao, Y.; Tan, H.; Li, H.; Lai, C. Ore-forming mechanism and physicochemical evolution of Gutaishan Au deposit, South China: Perspective from quartz geochemistry and fluid inclusions. *Ore Geol. Rev.* **2020**, *119*, 103382. [CrossRef]
5. Li, W.; Xie, G.Q.; Mao, J.W.; Zhang, Z.Y.; Fu, B.; Lu, S. Muscovite 40Ar/39Ar and in situ sulfur isotope analyses of the slate-hosted Gutaishan Au–Sb deposit, South China: Implications for possible Late Triassic magmatic-hydrothermal mineralization. *Ore Geol. Rev.* **2018**, *101*, 839–853. [CrossRef]
6. Li, W.; Cook, N.J.; Ciobanu, C.L.; Xie, G.; Wade, B.P.; Gilbert, S.E. Trace element distributions in (Cu)-Pb-Sb sulfosalts from the Gutaishan Au–Sb deposit, South China: Implications for formation of high fineness native gold. *Am. Mineral.* **2019**, *104*, 425–437. [CrossRef]
7. Li, W.; Cook, N.J.; Xie, G.Q.; Mao, J.W.; Ciobanu, C.L.; Li, J.W.; Zhang, Z.Y. Textures and trace element signatures of pyrite and arsenopyrite from the Gutaishan Au–Sb deposit, South China. *Miner. Depos.* **2019**, *54*, 591–610. [CrossRef]
8. Yu, J.G. Alteration features and prospecting direction in the Gutaishan gold deposit, Hunan. *Hunan Geol.* **1998**, *3*, 155–159. (In Chinese with English abstract)
9. Zhang, Z.Y.; Zhu, Q.Q.; Li, W.; Han, Y.X. Deep information of W–Au–Sb deposits in the Central Hunan Basin. *Miner. Depos.* **2014**, *33* (Suppl. S1), 491–492. (In Chinese)
10. Wu, J.C.; Wang, J.R.; Ou, J.; Wang, S.S.; Yang, S.F.; Li, Y.H. Fluid inclusions and isotopic geochemistry of the Baima–Longshan gold belt, Hunan: Implications for ore-forming fluids. *Miner. Resour. Geol.* **2007**, *21*, 673–678. (In Chinese)
11. Li, W.; Xie, G.Q.; Zhang, Z.Y.; Zhang, X.K. Constraint on the genesis of the Gutaishan gold deposit in central Hunan Province: Evidence from fluid inclusions and C–H–O isotopes. *Acta Petrol. Sin.* **2016**, *32*, 3489–3506, (In Chinese with English abstract).
12. Zhou, C.; Sun, J.; Guo, A.M.; Jia, P.Y.; Lu, W.; Wei, H.T.; Guo, D.; Cai, Y. A comparative study of the ore-forming fluids of the typical gold–antimony deposits along the Middle Xuefeng arc structural belt. *Geol. China* **2020**, *47*, 1241–1259. (In Chinese with English abstract)
13. Rusk, B. Cathodoluminescent textures and trace elements in hydrothermal quartz. In *Quartz: Deposits, Mineralogy and Analytics*; Götze, J., Möckel, R., Eds.; Springer: Berlin/Heidelberg, Germany, 2012; pp. 307–329.
14. Thomas, J.B.; Watson, E.B.; Spear, F.S.; Shemella, P.T.; Nayak, S.K.; Lanzirotti, A. TitaniQ under pressure: The effect of pressure and temperature on the solubility of Ti in quartz. *Contrib. Mineral. Petrol.* **2010**, *160*, 743–759. [CrossRef]
15. Liu, E.T.; Zhao, J.X.; Pan, S.Q.; Yan, D.T.; Wang, H. In-situ U-Pb Dating of Quartz: A Preliminary Study. *J. Earth Sci.* **2024**, *35*, 726–728. [CrossRef]
16. Lubben, J.D. Silicification Across the Betze-Post Carlin-Type Gold Deposit: Clues to Ore Fluid Properties and Sources, Northern Carlin Trend, Nevada. Master's Thesis, University of Nevada, Las Vegas, NV, USA, 2004.
17. Wang, X.; Qi, N.; Zhu, X.Y.; He, X.H.; Gu, H.W.; Deng, X.H. Magmatic to Hydrothermal Evolution of Bianjiadayuan Ag-Pb-Zn-Sn Deposit, NE China: A Quartz Texture and Trace Elements Study. *J. Earth Sci.* **2025**, *36*, 1493–1504. [CrossRef]
18. Rusk, B.G.; Lowers, H.A.; Reed, M.H. Trace elements in hydrothermal quartz: Relationships to cathodoluminescent textures and insights into vein formation. *Geology* **2008**, *36*, 547–550. [CrossRef]
19. Monecke, T.; Kempe, U.; Götze, J. Genetic significance of the trace element content in metamorphic and hydrothermal quartz: A reconnaissance study. *Earth Planet. Sci. Lett.* **2002**, *202*, 709–724. [CrossRef]
20. Agangi, A.; McPhie, J.; Kamenetsky, V.S. Magma chamber dynamics in a silicic LIP revealed by quartz: The Mesoproterozoic Gawler Range Volcanics. *Lithos* **2011**, *126*, 68–83. [CrossRef]
21. Götze, J.; Plötze, M.; Habermann, D. Origin, spectral characteristics and practical applications of the cathodoluminescence (CL) of quartz—A review. *Mineral. Petrol.* **2001**, *71*, 225–250. [CrossRef]
22. Landtwing, M.R.; Pettke, T. Relationships between SEM-cathodoluminescence response and trace-element composition of hydrothermal vein quartz. *Am. Mineral.* **2005**, *90*, 122–131. [CrossRef]
23. Mercer, C.N.; Reed, M.H.; Mercer, C.M. Time scales of porphyry Cu deposit formation: Insights from titanium diffusion in quartz. *Econ. Geol.* **2015**, *110*, 587–602. [CrossRef]
24. Wark, D.A.; Watson, E.B. TitaniQ: A titanium-in-quartz geothermometer. *Contrib. Mineral. Petrol.* **2006**, *152*, 743–754. [CrossRef]
25. Monnier, L.; Lach, P.; Salvi, S.; Melleton, J.; Bailly, L.; Béziat, D.; Monnier, Y.; Gouy, S. Quartz trace-element composition by LA-ICP-MS as proxy for granite differentiation, hydrothermal episodes, and related mineralization: The Beauvoir Granite (Echassières district), France. *Lithos* **2018**, *320–321*, 355–377. [CrossRef]

26. Wertich, V.; Leichmann, J.; Dosbaba, M.; Götze, J. Multi-stage evolution of gold-bearing hydrothermal quartz veins at the Mokrsko gold deposit (Czech Republic) based on cathodoluminescence, spectroscopic, and trace elements analyses. *Minerals* **2018**, *8*, 335. [CrossRef]
27. Krupp, R.E. Solubility of stibnite in hydrogen sulfide solutions, speciation, and equilibrium constants, from 25 to 350 °C. *Geochim. Cosmochim. Acta* **1988**, *52*, 3005–3015. [CrossRef]
28. Fu, S.; Hu, R.; Yin, R.; Yan, J.; Mi, X.; Song, Z.; Sullivan, N.A. Mercury and in situ sulfur isotopes as constraints on the metal and sulfur sources for the world's largest Sb deposit at Xikuangshan, southern China. *Miner. Depos.* **2020**, *55*, 1353–1364. [CrossRef]
29. Canfield, D.E. Isotope fractionation by natural populations of sulfate-reducing bacteria. *Geochim. Cosmochim. Acta* **2001**, *65*, 1117–1124. [CrossRef]
30. Ohmoto, H.; Goldhaber, M.B. Sulfur and carbon isotopes. In *Geochemistry of Hydrothermal Ore Deposits*; Barnes, H.L., Ed.; Wiley: New York, NY, USA, 1997; pp. 517–611.
31. Seal, R.R. Sulfur isotope geochemistry of sulfide minerals. *Rev. Mineral. Geochem.* **2006**, *61*, 633–677. [CrossRef]
32. Craddock, P.R.; Rouxel, O.J.; Ball, L.A.; Bach, W. Sulfur isotope measurement of sulfate and sulfide by high-resolution MC-ICP-MS. *Chem. Geol.* **2008**, *253*, 102–113. [CrossRef]
33. Yuan, H.; Liu, X.; Chen, L.; Bao, Z.; Chen, K.; Zong, C.; Li, X.C.; Qiu, J.W. Simultaneous measurement of sulfur and lead isotopes in sulfides using nanosecond laser ablation coupled with two multi-collector inductively coupled plasma mass spectrometers. *J. Asian Earth Sci.* **2018**, *154*, 386–396. [CrossRef]
34. Dai, Z.H.; Fu, S.L.; Liu, Y.F.; Meng, Y.M.; Bao, Z.A.; Hou, K.J.; Lan, T.G. A potential stibnite reference material for sulfur isotope determination by LA-MC-ICP-MS. *J. Anal. At. Spectrom.* **2024**, *39*, 216–226. [CrossRef]
35. Mason, P.R.D.; Košler, J.; de Hoog, J.C.M.; Sylvester, P.J.; Meffan-Main, S.K. In situ determination of sulfur isotopes in sulfur-rich materials by laser ablation multiple-collector inductively coupled plasma mass spectrometry (LA-MC-ICP-MS). *J. Anal. At. Spectrom.* **2006**, *21*, 177–186. [CrossRef]
36. Hou, L.; Peng, H.J.; Ding, J.; Zhang, J.R.; Zhu, S.B.; Wu, S.Y.; Wu, Y.; Ouyang, H.G. Textures and in situ chemical and isotopic analyses of pyrite, Huijiabao Trend, Youjiang basin, China: Implications for paragenesis and source of sulfur. *Econ. Geol.* **2016**, *111*, 331–353. [CrossRef]
37. Zhao, G. Jiangnan Orogen in South China: Developing from divergent double subduction. *Gondwana Res.* **2015**, *27*, 1173–1180. [CrossRef]
38. Qiu, L.; Yan, D.P.; Tang, S.L.; Wang, Q.; Yang, W.X.; Tang, X.; Wang, J. Mesozoic geology of southwestern China: Indosinian foreland overthrusting and subsequent deformation. *J. Asian Earth Sci.* **2016**, *122*, 91–105. [CrossRef]
39. Hu, R.Z.; Zhou, M.F. Multiple Mesozoic mineralization events in South China—An introduction to the thematic issue. *Miner. Depos.* **2012**, *47*, 579–588. [CrossRef]
40. Li, H.; Kong, H.; Zhou, Z.K.; Tindell, T.; Tang, Y.Q.; Wu, Q.H.; Xi, X.S. Genesis of the Banxi Sb deposit, South China: Constraints from wall-rock geochemistry, fluid inclusion microthermometry, Rb–Sr geochronology, and H–O–S isotopes. *Ore Geol. Rev.* **2019**, *115*, 103162. [CrossRef]
41. Ma, D.S.; Pan, J.Y.; Xie, Q.L. Ore sources of Sb (Au) deposits in central Hunan: II. Evidence of isotopic geochemistry. *Miner. Depos.* **2003**, *22*, 78–87. (In Chinese)
42. Peng, J.T. Hunan Xuefeng area gold metallogenic evolution mechanism discussion. *Tecton. Metallog.* **1999**, *23*, 144–151. (In Chinese)
43. Wang, F.R.; Quan, Z.Y.; Hu, N.Y.; Li, Y.P. Metallogenic conditions and distribution-enrichment patterns of gold deposits in Hunan Province. *Hunan Geol.* **1993**, *12*, 163–170. (In Chinese)
44. Wang, G. Geological-Geochemical Characteristics of Caledonian Granitoids and Its Geological Significance: Taking Baimashan, Xuefengshan, Hongxiaqiao Plutons as Examples. Master's Thesis, Central South University, Changsha, China, 2013; pp. 10–70. (In Chinese with English abstract)
45. Chen, W.; Chen, P.; Huang, H.; Ding, X.; Sun, T. Chronological and geochemical studies of granite and enclave in Baimashan pluton, Hunan, South China. *Sci. China Ser. D Earth Sci.* **2007**, *50*, 1606–1627. [CrossRef]
46. Luo, Z.G.; Wang, Y.J.; Zhang, F.F.; Zhang, A.M.; Zhang, Y.Z. LA-ICPMS zircon U–Pb dating for Baimashan and Jintan Indosinian granitic plutons and its petrogenetic implications. *Geotecton. Metallog.* **2010**, *34*, 282–290.
47. Liu, J.Q.; Yuan, X.; Zhan, Z.; Lin, J.S.; Feng, W.M.; Huang, X.P. The geochronologic characteristics of Baimashan granite in western Hunan Province and its geotectonic significance. *Earth Sci. Front.* **2013**, *20*, 25–35.
48. Kang, R.H. Analysis of Exploration Perspectives of Gold–Antimony Deposits in the Baimashan–Longshan EW-Striking Structural Zone, Hunan Province. *Geol. Miner. Resour. South China* **2002**, *18*, 57–61. (In Chinese with English abstract) [CrossRef]
49. Jiang, C.; Xie, B.W.; Duan, A.J.; Huang, X.J.; Ai, G.; Liu, W. Study on Geological Characteristics and Prospecting Direction of No.3 Vein in Gutaishan Gold-antimony Deposit, Hunan Province. *Mod. Min.* **2024**, *40*, 49–53+61.

50. Jochum, K.P.; Willbold, M.; Raczek, I.; Stoll, B.; Herwig, K. Chemical Characterisation of the USGS Reference Glasses GSA-1G, GSC-1G, GSD-1G, GSE-1G, BCR-2G, BHVO-2G and BIR-1G Using EPMA, ID-TIMS, ID-ICP-MS and LA-ICP-MS. *Geostand. Geoanal. Res.* **2005**, *29*, 285–302. [CrossRef]
51. Liu, Y.; Hu, Z.; Gao, S.; Günther, D.; Xu, J.; Gao, C.; Chen, H. In situ analysis of major and trace elements of anhydrous minerals by LA-ICP-MS without applying an internal standard. *Chem. Geol.* **2008**, *257*, 34–43. [CrossRef]
52. Chen, L.; Chen, K.; Bao, Z.; Liang, P.; Sun, T.; Yuan, H. Preparation of standards for in situ sulfur isotope measurement in sulfides using femtosecond laser ablation MC-ICP-MS. *J. Anal. At. Spectrom.* **2017**, *32*, 107–116. [CrossRef]
53. Bao, Z.; Chen, L.; Zong, C.; Yuan, H.; Chen, K.; Dai, M. Development of pressed sulfide powder tablets for in situ sulfur and lead isotope measurement using LA-MC-ICP-MS. *Int. J. Mass Spectrom.* **2017**, *421*, 255–262. [CrossRef]
54. Fu, S.; Lan, Q.; Yan, J. Trace element chemistry of hydrothermal quartz and its genetic significance: A case study from the Xikuangshan and Woxi giant Sb deposits in southern China. *Ore Geol. Rev.* **2020**, *126*, 103732. [CrossRef]
55. Zhu, Y.N.; Peng, J.T. Infrared microthermometric and noble gas isotope study of fluid inclusions in ore minerals at the Woxi orogenic Au–Sb–W deposit, western Hunan, South China. *Ore Geol. Rev.* **2015**, *65*, 55–69. [CrossRef]
56. Müller, A.; Wiedenbeck, M.; van den Kerkhof, A.M.; Kronz, A.; Simon, K. Trace elements in quartz—A combined electron microprobe, secondary ion mass spectrometry, laser ablation ICP-MS, and cathodoluminescence study. *Eur. J. Mineral.* **2003**, *15*, 747–763. [CrossRef]
57. Müller, A.; Koch-Müller, M. Hydrogen speciation and trace element contents of igneous, hydrothermal and metamorphic quartz from Norway. *Mineral. Mag.* **2009**, *73*, 569–583. [CrossRef]
58. Götte, T.; Ramseyer, K. Trace element characteristics, luminescence properties and real structure of quartz. In *Quartz: Deposits, Mineralogy and Analytics*; Rusk, B.G., Ed.; Springer: Berlin/Heidelberg, Germany, 2012; pp. 265–285.
59. Griffiths, J.H.E.; Owen, J.; Ward, I.M. Paramagnetic resonance in neutron-irradiated diamond and smoky quartz. *Nature* **1954**, *173*, 439–440. [CrossRef]
60. Walsby, C.J.; Lees, N.S.; Claridge, R.F.; Weil, J.A. The magnetic properties of oxygen-hole aluminum centres in crystalline SiO_2. VI: A stable AlO_4/Li centre. *Can. J. Phys.* **2003**, *81*, 583–598. [CrossRef]
61. Götze, J. Chemistry, textures and physical properties of quartz—Geological interpretation and technical application. *Mineral. Mag.* **2009**, *73*, 645–671. [CrossRef]
62. Rusk, B.G.; Reed, M.H.; Dilles, J.H.; Kent, A.J. Intensity of quartz cathodoluminescence and trace-element content in quartz from the porphyry copper deposit at Butte, Montana. *Am. Mineral.* **2006**, *91*, 1300–1312. [CrossRef]
63. Weil, J.A. A review of electron spin spectroscopy and its application to the study of paramagnetic defects in crystalline quartz. *Phys. Chem. Miner.* **1984**, *10*, 149–165. [CrossRef]
64. Miyoshi, N.; Yamaguchi, Y.; Makino, K. Successive zoning of Al and H in hydrothermal vein quartz. *Am. Mineral.* **2005**, *90*, 310–315. [CrossRef]
65. Lehmann, K.; Berger, A.; Götte, T.; Ramseyer, K.; Wiedenbeck, M. Growth related zonations in authigenic and hydrothermal quartz characterized by SIMS-, EPMA-, SEM-CL-, and SEM-CC-imaging. *Mineral. Mag.* **2009**, *73*, 633–643. [CrossRef]
66. Lehmann, K.; Pettke, T.; Ramseyer, K. Significance of trace elements in syntaxial quartz cement, Haushi Group sandstones, Sultanate of Oman. *Chem. Geol.* **2011**, *280*, 47–57. [CrossRef]
67. Pokrovski, G.S.; Schott, J. Thermodynamic properties of aqueous Ge (IV) hydroxide complexes from 25 to 350 °C: Implications for the behavior of germanium and the Ge/Si ratio in hydrothermal fluids. *Geochim. Cosmochim. Acta* **1998**, *62*, 1631–1642. [CrossRef]
68. Blankenburg, H.J.; Götze, J.; Schulz, H. *Quarzrohstoffe*; Deutscher Verlag für Grundstoffindustrie: Leipzig-Stuttgart, Germany, 1994; p. 296.
69. Götze, J.; Pan, Y.; Müller, A. Mineralogy and mineral chemistry of quartz: A review. *Mineral. Mag.* **2021**, *85*, 639–664. [CrossRef]
70. Rottier, B.; Casanova, V. Trace element composition of quartz from porphyry systems: A tracer of the mineralizing fluid evolution. *Miner. Depos.* **2021**, *56*, 843–862. [CrossRef]
71. Peterková, T.; Dolejš, D. Magmatic-hydrothermal transition of Mo-W-mineralized granite-pegmatite-greisen system recorded by trace elements in quartz: Krupka district, Eastern Krušné hory/Erzgebirge. *Chem. Geol.* **2019**, *523*, 179–202. [CrossRef]
72. Breiter, K.; Badanina, E.; Ďurišová, J.; Dosbaba, M.; Syritso, L. Chemistry of quartz—A new insight into the origin of the Orlovka Ta-Li deposit, Eastern Transbaikalia, Russia. *Lithos* **2021**, *348–349*, 105206. [CrossRef]
73. Obolensky, A.A.; Gushchina, L.V.; Borisenko, A.S.; Borovikov, A.A.; Pavlova, G.G. Antimony in hydrothermal processes: Solubility, conditions of transfer, and metal-bearing capacity of solutions. *Russ. Geol. Geophys.* **2007**, *48*, 992–1001. [CrossRef]
74. Biver, M.; Shotyk, W. Stibnite (Sb_2S_3) oxidative dissolution kinetics from pH 1 to 11. *Geochim. Cosmochim. Acta* **2012**, *79*, 127–139. [CrossRef]
75. Ohmoto, H. Systematics of sulfur and carbon isotopes in hydrothermal ore deposits. *Econ. Geol.* **1972**, *67*, 551–578. [CrossRef]
76. Rees, C.E.; Jenkins, W.J.; Monster, J. The sulphur isotopic composition of ocean water sulphate. *Geochim. Cosmochim. Acta* **1978**, *42*, 377–381. [CrossRef]
77. Rao, J.R.; Wang, J.H.; Cao, Y.Z. Deep structure in Hunan. *Hunan Geol.* **1993**, *12*, 1–101. (In Chinese with English abstract)

78. Peng, J.; Hu, R.; Zhao, J.; Fu, Y.; Lin, Y. Scheelite Sm-Nd dating and quartz Ar-Ar dating for Woxi Au–Sb-W deposit, western Hunan. *Chin. Sci. Bull.* **2003**, *48*, 2640–2646. [CrossRef]
79. Goldfarb, R.J.; Baker, T.; Dubé, B.; Groves, D.; Hart, C.; Gosselin, P. Distribution, character and genesis of gold deposits in metamorphic terranes. In *Economic Geology 100th Anniversary Volume*; Hedenquist, J.W., Thompson, J.F.H., Goldfarb, R.J., Richards, J.P., Eds.; Society of Economic Geologists, Inc.: Littleton, CO, USA, 2005; pp. 407–450.
80. Phillips, G.N.; Powell, R. Formation of gold deposits: A metamorphic devolatilization model. *J. Metamorph. Geol.* **2010**, *28*, 689–718. [CrossRef]
81. Tang, Y.; Wang, Q.; Yang, Y.L.; Zhou, Y.L.; Cui, X.D.; Zou, H. Petrogenesis and geodynamic implications of the Baimashan granitic complex in central Hunan, South China. *Geol. J.* **2022**, *57*, 4718–4745. [CrossRef]
82. Williams-Jones, A.E.; Norman, C. Controls of mineral parageneses in the system Fe-Sb-SO. *Econ. Geol.* **1997**, *92*, 308–324. [CrossRef]
83. Robert, F.; Poulsen, K.H.; Cassidy, K.F.; Hodgson, C.J. *Gold Metallogeny of the Superior and Yilgarn Cratons*; Society of Economic Geologists: Littleton, CO, USA, 2005.
84. Thébaud, N.; Sugiono, D.; LaFlamme, C.; Miller, J.; Fisher, L.; Voute, F.; Tessalina, S.; Sonntag, I.; Fiorentini, M. Protracted and polyphased gold mineralisation in the Agnew district (Yilgarn craton, Western Australia). *Precambrian Res.* **2018**, *310*, 291–304. [CrossRef]
85. Moncada, D.; Rimstidt, J.D.; Bodnar, R.J. How to form a giant epithermal precious metal deposit: Relationships between fluid flow rate, metal concentration of ore-forming fluids, duration of the ore-forming process, and ore grade and tonnage. *Ore Geol. Rev.* **2019**, *113*, 103066. [CrossRef]
86. Sasmaz, A.; Sukach, V.; Bondarenko, S.; Aleksiienko, H.; Erfanian Kaseb, H.; Sasmaz, B.; Kurylo, S.; Hrinchenko, O.; Somka, V.; Voudouris, P. Newly Identified Au-Ag-Bi-Te Mineralization in the Aydindere Skarn Fe and Cu Deposit, Giresun, NE Turkey: Implications of Gold Mineralization during Retrograde Skarn Evolution. *J. Earth Sci.* **2025**, *36*, 543–561. [CrossRef]
87. Hou, X.N.; Fu, S.L.; Kong, H.; Liu, B.; Tang, Y.W.; Huang, J.G. Is there superimposed mineralization occurring within the Longshan Sb-Au deposit, South China? A perspective from U-Pb dating of apatite and in-situ S isotopes of pyrite and stibnite. *Ore Geol. Rev.* **2025**, *181*, 106631. [CrossRef]

Disclaimer/Publisher's Note: The statements, opinions and data contained in all publications are solely those of the individual author(s) and contributor(s) and not of MDPI and/or the editor(s). MDPI and/or the editor(s) disclaim responsibility for any injury to people or property resulting from any ideas, methods, instructions or products referred to in the content.